Anomalous Thickness Dependence of the Vortex Pearl Length in Few-Layer NbSe$_2$

Nofar Fridman[1,2], Tomer Daniel Feld[1,2], Avia Noah[1,2], Ayelet Zalic[1,2], Maya Markman[1,2], T.R Devidas[1,2], Yishay Zur[1,2], Einav Grynszpan[1,2], Alon Gutfreund[1,2], Itay Keren[1,2], Atzmon Vakahi[2], Sergei Remennik[2], Kenji Watanabe[3], Takashi Taniguchi[3], Martin Emile Huber[4], Igor Aleiner[5], Hadar Steinberg[1,2], Oded Agam[1], Yonathan Anahory[1,2]

[1] The Racah Institute of Physics, The Hebrew University, Jerusalem, 9190401, Israel
[2] Center for Nanoscience and Nanotechnology, Hebrew University of Jerusalem, Jerusalem, 9190401, Israel
[3] Research Center for Electronic and Optical Materials, National Institute for Materials Science, 1-1 Namiki, Tsukuba 305-0044, Japan
[4] Departments of Physics and Electrical Engineering, University of Colorado Denver, Denver, CO 80217, USA
[5] Google Quantum AI, Santa Barbara, CA, USA

Abstract

The coexistence of multiple types of orders is a common thread in condensed matter physics and unconventional superconductors. The nature of superconducting orders may be unveiled by analyzing local perturbations such as vortices. For thin films, the vortex magnetic profile is characterized by the Pearl-length Λ, which is inversely proportional to the 2D superfluid density; hence, normally, also inversely proportional to the film thickness, d. Here we employ the scanning SQUID-on-tip microscopy to measure Λ in NbSe$_2$ flakes with thicknesses ranging from $N = 3$ to 53 layers. For $N > 10$, we find the expected dependence $\Lambda \propto 1/d$. However, six-layer films show a sharp increase of Λ deviating by a factor of three from the expected value. This value remains fixed for $N = 3$ to 6. This unexpected behavior suggests the competition between two orders; one residing only on the first and last layers of the film while the other prevails in all layers.

Introduction

Superconductivity in the presence of competing or intertwined order parameters has generated much interest over the last decades. Detecting the presence of an additional order parameter and determining its influence on superconductivity is crucial in unveiling the pairing mechanism. In particular, order-parameter competition could involve two superconducting order parameters with different pairing symmetries[1] or a single superconducting channel and an order parameter related to another degree of freedom, such as charge density wave[2,3] or spin density wave.[4]

Although usually discussed in the context of high-temperature superconductors,[5,6] competing orders are also relevant to many other layered materials, such as twisted bilayer graphene[7] and NbSe$_2$.[1] Moreover, in the case of thin films with few atomic layers, the competition between distinct order parameters residing on the surface and in the bulk also becomes a possibility. This is due to the disparity in properties exhibited by the surface and bulk regions, notably exemplified by the presence of Rashba spin-orbit coupling on the surface.[8] However, as far as we are aware, the examination of competition between surface and bulk order parameters, both experimentally and theoretically, has not been documented in prior studies. In this work, such a competition is uncovered through measurements of the magnetic field profile of superconducting vortices in NbSe$_2$. NbSe$_2$ is a layered superconductor which sustains superconductivity with $T_c > 4.2$ K for any thickness above 3 layers, and thus is uniquely suitable for such an experiment.

Superconducting vortices are often exploited as local perturbations used to probe the properties of the order parameter.[9–12] Vortices consist of a core where the superconductivity is locally suppressed on the scale of the coherence length ξ where the magnetic field can penetrate. This field is screened by the surrounding superconducting currents and results in magnetic flux quantization. In bulk superconductors, the magnetic field is screened exponentially with a characteristic scale of the London penetration depth λ_L. By contrast, for a film of thickness $d < \lambda_L$, screening is less effective and is governed by the Pearl length $\Lambda = 2\lambda_L^2/d$.[13–15] In this limit, the magnetic field decays as $1/\Lambda r$ near the vortex core and Λ/r^3 for distances greater than Λ, where r is the distance from the vortex's center. Therefore, near the vortex core, there is no characteristic length scale for the magnetic field screening. In this work, we measure the Pearl length, which is a fundamental characterizer of superconductors that is highly sensitive to variation of the two-dimensional superfluid density. This sensitivity is particularly important when studying phase transitions that involve changes in the superconducting order, as such transitions naturally alter the superfluid density.

We have measured the thickness dependence of the Pearl length in NbSe$_2$ flakes with thickness ranging from $N = 3$ to 53 layers. For this purpose we employ a highly sensitive microscopy technique of SQUID-on-tip[16,17] (Figure 1) coupled to a tuning fork designed to measure gradients in minute magnetic signals emitted by a vortex, particularly in cases where the Pearl length significantly exceeds the size of micron-scale flakes. Our data presents the anticipated $1/d$ dependence for flakes of thicknesses $N \gtrsim 10$ layers. However, strikingly, Λ largely deviate from the expected $1/d$ dependence for thinner films. Such deviation has not been previously reported in NbSe$_2$ neither in transport[18] nor in tunneling[3,9,19–21] studies. We suggest that the sharp jump in Λ can be attributed to the competition between bulk and surface superconductivity.
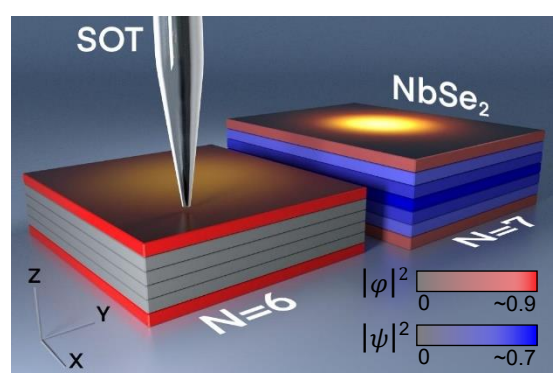
Figure 1: Schematic diagram of the experimental setup. Two NbSe₂ flakes with $N = 6$ and 7 layers. SQUID-on-tip (SOT) magnetic images of vortices representing the magnitude of the out-of-plane component of the magnetic field $B_z(h, \boldsymbol{r})$ are overlaid on the top surface, where h is the distance of the tip from the surface and $\boldsymbol{r} = (x, y)$ is the in-plane coordinate). The contour of each layer is colored according to the superconducting order parameters: ψ (blue) residing in all layers, and φ (red) is a different superconducting order parameter confined to the surface. The color intensity encodes the amplitude of each order parameter, where grey represent the normal state $|\psi| = 0$. For $N = 7$, the two order parameters are finite, while for $N = 6$, $|\psi| = 0$, while $|\varphi|$ remains finite and confined to the first and last layer.

Results:

NbSe₂ was mechanically exfoliated to obtain flakes with thicknesses ranging from $N = 3$ to 53 layers ($d = 1.9$ to 33 nm). To prevent sample degradation, thin flakes with $N \leq 14$ layers were encapsulated with h-BN from both sides (see Methods). Figures 2a,b depict representative optical images of thin films, showcasing the presence of atomically flat terraces. The number of layers, which corresponds to the thickness, is indicated for each observed area. For thin flakes ($N \leq 14$ layers), sample thickness was measured using cross-sectional scanning transmission electron microscopy (STEM), as described in the Methods and shown in Supplementary Figure 1. For thicker samples with $N > 14$ layers, the thickness was measured using an atomic force microscope (AFM). Energy-dispersive X-ray spectroscopy (EDS) analysis was performed on the flakes ($N \leq 14$ layers) and showed no surface contamination (Supplementary Figure 2).

The samples are mounted in a scanning SOT microscope to conduct magnetic imaging. In particular, we image the out-of-plane component of the magnetic field $B_z(h, \boldsymbol{r})$ at the surface of superconducting NbSe₂ in the presence of vortices at 4.2 K (Fig. 1), where h is the distance of the tip from the surface and $\boldsymbol{r} = (x, y)$ is the in-plane coordinate. Vortices are visually identified as bright regions in the acquired images (see Fig. 1 and 2c). To ensure non-overlapping signals from individual vortices, we adjusted the external magnetic field $\mu_0 H_z \sim 1$ mT, that controls the vortex density. The positions of the vortices measured at different magnetic fields are marked with orange dots in Fig. 2a,b (see also Supplementary Figure 3).

We commence by clarifying our capacity to extract the Pearl length even in cases where it considerably surpasses the flake size. The magnetic field profile of the Pearl vortex exhibits a characteristic gradual transition from the short-distance asymptotic behavior, described by $1/(\Lambda r)$, when $h \ll r \ll \Lambda$ to the long-distance behavior of Λ/r^3 when $r \gg \Lambda$. Examples of such profiles are presented in Fig. 2d for $h = 260$ nm with $\Lambda = 1.5$ μm and $\Lambda = 100$ μm and plotted for a typical SOT field of view ($|r| \leq 1.1$ μm). For this region of interest, $h \ll r \ll \Lambda$, both profiles are governed by the same power-law decay. Therefore, the two profiles differ solely by their magnitude, which is inversely proportional to Λ. The slow $1/r$ decay implies that magnetic fields resulting from neighboring vortices and the Meissner current associated with the sample's edges add up to an approximately constant background. This background can be effectively eliminated by measuring the gradient of the signal yielding a localized signal from which the Pearl length can be extracted with an error of order $(h/L)^2$, where L is the typical size of the flake or the distance to a neighboring vortex (see Supplementary Note 1). As we typically measure at $h \lesssim 0.4$ μm and L is typically larger than 1 μm, this error is small. To substantiate this result, we fit simulated isolated vortices and compare them with fits for vortices surrounded by randomly distributed vortices at a typical distance we encounter in experimental conditions (~ 2 μm). Our results, presented in Supplementary Figure 4, show that the influence of these additional vortices on Λ is up to 10%. Thus, when the magnetic field sufficiently weak, it is feasible to measure Pearl lengths in the range of a few hundred microns, even with a limited field of view of just a few microns. The capability to measure screening lengths of such magnitude is essential for the conclusions drawn in this work.
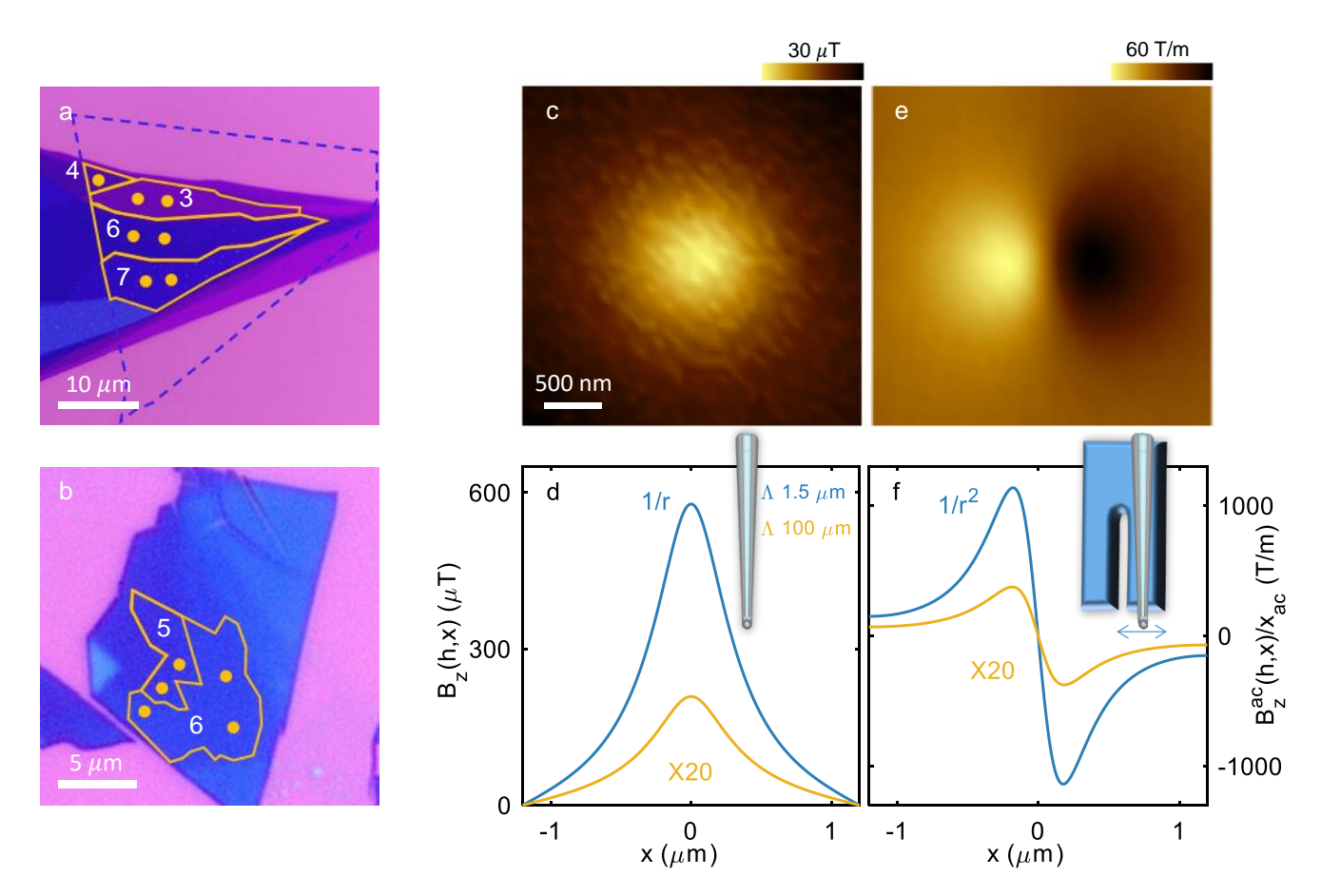
Figure 2: Pearl model and SQUID-on-tip images of NbSe₂ at 4.2K (a,b) Optical images of the ultra-thin flakes and the locations of the imaged vortices. The numbers indicate the number of layers N, and orange lines outline the terraces' edges. (**a**) The blue dashed line shows the area covered with top and bottom hBN. (**b**) The entire field of view is encapsulated with top and bottom hBN (**c**) SQUID-on-tip (SOT) image of the out-of-plane component of the magnetic field $B_z(h, \boldsymbol{r})$ of an isolated vortex located in the $N = 7$ layer region shown in panel **a**. (**d**) Calculated magnetic profile $B_z(h, x)$ of vortices using the Pearl model with Pearl length $\Lambda =$ 1.5 (blue) and 100 μm (yellow). Both profiles decay with the same power law ($1/\Lambda r$) for $r \ll \Lambda$. (inset) Illustration of a SOT scanning the surface monotonically as opposed to **f**. (**e**) The same vortex as in **c**, measured while the tip oscillates along the x axis. The image shows the field component oscillating in phase with the SQUID loop $B_z^{ac}(h, \boldsymbol{r})$ divided by the motion amplitude x_{ac} resulting in spatial derivative of the image shown in **c** along the x axis. (**f**) Same as **d** but showing the spatial derivative along the x axis $B_z^{ac}(h, x)/x_{ac}$. (inset) Illustration of the SOT coupled to a tuning fork oscillating along the x axis (blue double-headed arrow).

To measure the gradient of the out-of-plane component of the magnetic field, $B_z(h, \boldsymbol{r})$, we mechanically couple the SOT to a tuning fork, as shown in Figure 2f. The tuning fork is set to oscillate, resulting in a periodic lateral motion of the SQUID loop at a frequency of approximately 32 kHz, as indicated by the blue double-headed arrow in the inset of the Figure. When the amplitude of the tuning fork oscillation is small, the in-phase ac signal, $B_z^{ac}(h, \boldsymbol{r})$, is proportional to the gradient of the corresponding dc signal along a chosen direction. Setting the x axis along this direction, $B_z^{ac}(h, \boldsymbol{r}) \cong x_{ac}\, dB_z(h, \boldsymbol{r})/dx$, where x_{ac} is the oscillation amplitude of the SQUID loop. Using an independent measurement of the oscillation amplitude (see Methods and Supplementary Note 2), we are able to deduce the spatial derivative of the static signal $B_z(h, \boldsymbol{r})$, shown in Fig. 2e. Typically we set $x_{ac} \lesssim 100$ nm, which yields large signal while keeping the following approximation $B_z^{ac}(h, \boldsymbol{r}) \cong x_{ac}\, dB_z(h, \boldsymbol{r})/dx$ within our experimental uncertainty. Moreover, by conducting measurements at a frequency of 32 kHz, we are able to effectively eliminate the $1/f$ noise, which is typically at least two orders of magnitude higher below 1 kHz.[16,17]
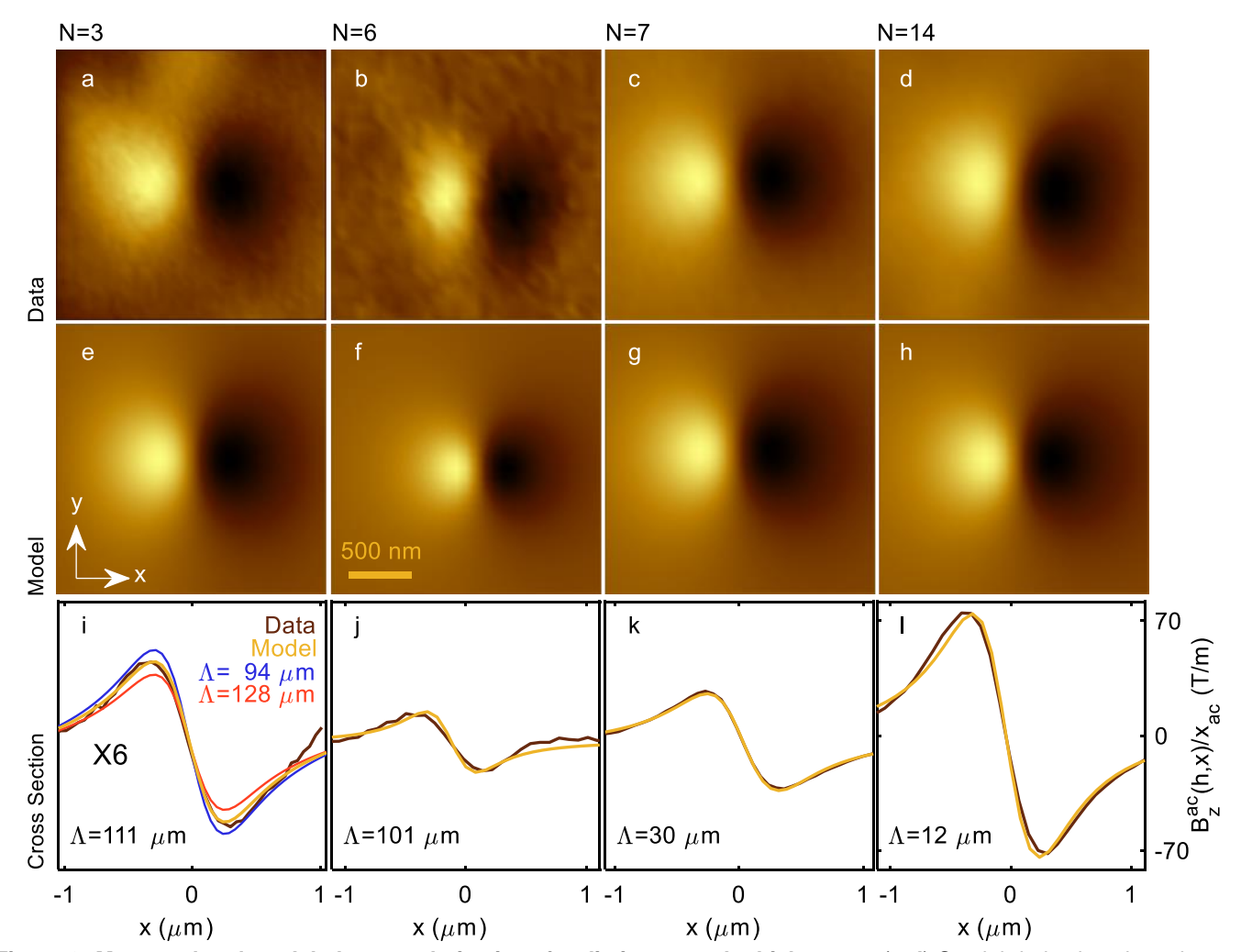
Figure 3: Measured and modeled vortex derivatives for distinct sample thicknesses (**a-d**) Spatial derivative along the x axis of the out-of-plane component of magnetic field $B_z^{ac}(h,\boldsymbol{r})/x_{ac}$ of a vortex located in a region of $N = 3$ **a**, 6 **b**, 7 **c**, and 14 **d** layers, where h is the distance from the tip-to-surface distance and $\boldsymbol{r} = (x,y)$ is the in-plane coordinate. Images acquired from $h = 360$ **a**, 360 **b** 260 **c**, and 360 **d** nm (**e-h**) Calculated theoretical magnetic image to obtain the best fit of the images shown in **a-d**. The Pearl lengths obtained are $\Lambda = 111$ **e**, 101 **f**, 30 **g**, and 12 **h** μm (**i-l**) Profile of the experimental data $B_z^{ac}(h,x)/x_{ac}$ (brown), and the calculated vortex (yellow). (**i**) Calculated vortex profile with $\Lambda = 94$ (red), 128 (blue) μm, which is a $\pm15\%$ deviation from the best fit, all curves are multiplied by a factor 6 for clarity.

Figures 3a-d display typical images of the spatial derivative along the x axis of the out-of-plane component of the magnetic field ($B_z^{ac}(h,\boldsymbol{r})/x_{ac}$) measured for various thicknesses ($N = 3,6,7$, and 14 layers). Figures 3e-h show the best fits achieved for each image to the Pearl model. This model requires two parameters, the height h and the Pearl length Λ. We determine h by sensing the sample surface with the tuning fork, as in an AFM, then retract a known amount, leaving Λ as our sole fitting parameter. The uncertainty on the measurement of h is 15 nm, which propagates to an uncertainty in the Pearl length of 8%-10% (Supplementary Note 3). In addition, we take into account our finite SOT resolution by convoluting the modeled image with a circle corresponding to the SQUID's diameter, which we determine by measuring the field period of the critical current oscillations[16,17]. To demonstrate the good agreement between fits and measurements, we show the cross-sections of derivatives of the model and the $B_z^{ac}(h,\boldsymbol{r})/x_{ac}$ signal along the x axis of the image (Fig. 3, i-l). From these fits we obtain $\Lambda = 111, 101, 30$, and 12 μm for $N = 3,6,7$, and 14, respectively. Notably, the measured signal magnitude is approximately twice as large for $N = 6$ compared to $N = 3$, despite obtaining similar Λ values for both cases. The difference of the signals is attributed to the difference in the tip height at which the measurement was conducted: $h = 360 \pm 15$ and 260 ± 15 nm for $N = 3$ and 6, respectively. The nearly constant value of Λ for two different thicknesses manifests a puzzling deviation from the expected $1/d$ dependence.

Figure 4 summarizes the measured values of the Pearl length Λ as a function of the thickness d ranging from $N = 3$ to 53 layers plotted on a logarithmic scale. According to the Pearl model, this plot is expected to exhibit a slope of -1 (representing the d^{-1} dependence of the Pearl length) along with an offset determined by the London penetration depth λ_L. Indeed, for $N \gtrsim 10$ layers, such dependence is observed, enabling us to estimate $\lambda_L = 230$ nm in good agreement with bulk value $\lambda_L = 200$ nm measured at 4.2 K[22–25]. Notice that, for thicker films, the thickness was measured with AFM, and the flakes were not encapsulated. Consequently, the uncertainty on the thickness is larger, which explains partially the scatter of the data points around $1/d$.

For $N = 6$, we observe a drastic increase in Λ, to 101 μm, which is three times larger than the expected value of 28 μm according to Pearl model. Moreover, Λ remains surprisingly constant, within 100 ± 15 μm, for $N = 3,4,5$, and 6 layers.

However, take note that in a different sample with $N = 6$, we obtained a significantly different value of $\Lambda = 39$ μm. This value is somewhat closer to the expected value from Pearl's model of 28 μm. These findings suggest that near a critical thickness of $N = 6$, where the system undergoes a phase transition, finite size effects are significant.
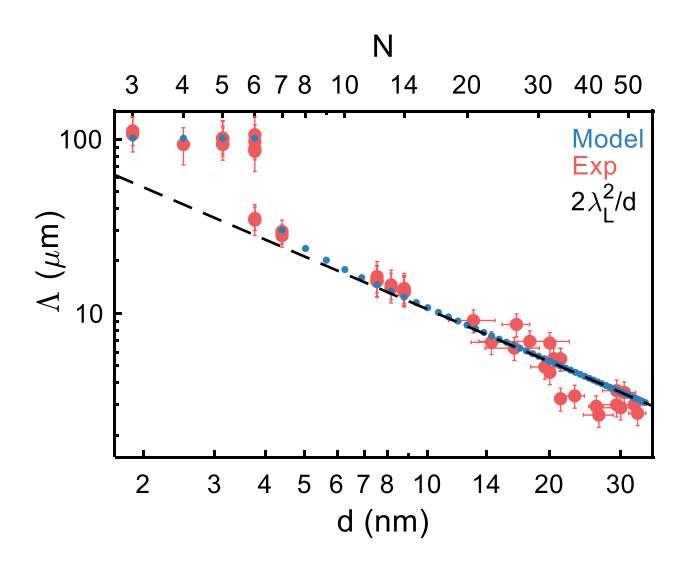

Figure 4: Thickness dependence of the Pearl length Measured Pearl length Λ (red dots) obtained from SOT images and the best fit to our phenomenological model (blue dots). The black dashed line represents Pearl length thickness dependence according to the Pearl model considering $\lambda_L = 230$ nm. The error bars represent the total uncertainty resulting from the systematical and statistical (one standard deviation) uncertainties as described in Supplementary Note 3 and Supplementary Figures 4,5. The sudden suppression of bulk superconductivity ψ depicted in Figure 1 is reflected by the sharp increase of Λ at $N = 6$ layers.

Two key features characterize the measured Pearl length dependence on the film thickness. The constant value of Λ below the critical thickness, and the sharp jump near $N = 6$. In what follows, we discuss potential experimental issues, and explain why their impact on our findings is negligible. Consider first the issue of sensitivity limitations. In Figure 3i, we compare the profile of the image measured in Figure 3a with three simulated profiles. The best fit (in yellow) and two other profiles obtained by changing Λ by $\pm 15\%$ (blue and red). The figure demonstrates that it is possible to distinguish variations in Λ of the order of 15%, given our measurement sensitivity (Supplementary Note 3). This resolution is largely sufficient when compared to our claims. Another potential issue is the disorder and surface roughness, which might introduce possible limitation on the measured film thickness. To exclude this mechanism, cross-sectional STEM images were taken (Supplementary Figure 1) to ensure the crystal quality and asses contamination for all thin films ($N \leq 14$). The flakes were found to be atomically flat without traces of contamination over micron-size terraces where vortices were imaged.

Discussion

The sharp jump of Λ near $N = 6$ indicates a sharp reduction in the total superfluid density. NbSe$_2$ is known to be a two-band superconductor[26], with a larger energy band associated with the Nb orbitals, and the lower energy band with the Se orbitals. Hence a possible explanation for this reduction is the suppression of one of the bands with the thickness of the film.[18,20,21,27,28] Although that could explain the jump in Λ, it does not account for the saturation of Λ in thinner films as the $1/d$ dependence should persist albeit with a different offset. Moreover, in NbSe$_2$, the spectral signature of the Se-derived band disappears gradually at films in the $d \sim 10$ to 20 nm thickness range,[21] well above the thickness of 3.5 nm ($N = 6$) where we observe the transition.

The distinctive behavior of Λ presented in Fig. 4 suggests the presence of a phase transition wherein a partial disappearance of superconductivity occurs as the film thickness diminishes, thus leading to a notable jump in the Pearl length. At the same time, the saturation in the Pearl length implies the persistence of the superfluid density independent of the film thickness. This feature indicates that the remaining superconducting order parameter is confined in specific layers, and therefore unaffected by the film thickness. Thus, the order parameter, which is suppressed for thinner films, prevails elsewhere for $N > 6$.

The observed jump in the Pearl length dependence as a function of the number of layers in the film, $\Lambda(N)$, can be naturally explained within the framework of the two-component Ginzburg-Landau description, in which φ and ψ, represent superconducting order parameters belonging to different superconducting classes. In this description, the Pearl length is given by the sum of two contributions,

$$\frac{1}{\Lambda(N)} = N\frac{|\psi|^2}{\Lambda_b} + \frac{|\varphi|^2}{\Lambda_s},$$

where Λ_b is a length scale characterizing the bulk, while Λ_s is associated with the surface. The order parameters φ and ψ, are determined by minimization of the dimensionless energy density of an effectively two-dimensional system:

$$F_N = n^*|\varphi|^2\left(-2+|\varphi|^2+\mu|\psi|^2\right) + N|\psi|^2\left(-2+|\psi|^2\right),$$

where n^* and μ, are fitting parameters that control the competition between the two order parameters. The length scales, Λ_b and Λ_s, are uniquely determined from the asymptotic limits of the Pearl length at large and small film thicknesses. They are found to be: $\Lambda_b = 2\lambda_L^2/a$ and $\Lambda_s = 0.6\Lambda_b$, where $\lambda_L = 230$ nm is the bulk London penetration depth, while $a = 0.63$ nm is the spacing between neighboring layers. The two other fitting parameters, n^* and μ, are chosen such that $\Lambda(N)$ follows the data points and the system undergoes a first-order phase transition at thickness of approximately $N \sim 6$ layers. This transition transforms the system from a phase where both ψ and φ are non-zero ($N \geq 7$) to a phase where ψ vanishes while φ remains non zero ($N \leq 6$). The experimental data is perfectly described by $n^* = 6.5$ and $\mu = 1.9$, as shown in Fig. 4. In this model the energy associated with the φ-component is independent of the number of layers, N, therefore it is associated with a contribution coming from the surface of the film (i.e., the first and last layers). Furthermore, the experimental data does not corroborate the presence of a term proportional to $\varphi^*\psi + \varphi\psi^*$ in the free energy. Hence, ψ and φ must belong distinct irreducible representations of the system's superconducting symmetry group, linked to the point groups D_{3h} and D_{3d} for films with an odd or even number of layers, respectively. These irreducible representations are both one-dimensional; otherwise, the system should exhibit an additional type of symmetry breaking. The sensitivity of our measurements is insufficient for unveiling such a symmetry-breaking.

The phenomenological model proposed herein assumes the presence of a superconducting order parameter localized near the sample surface, distinct from that of the bulk. This order parameter may originate from various factors, such as a strong Rashba spin-orbit coupling at the surface or the presence of strain induced by lattice mismatch between hexagonal h-BN and NbSe$_2$. Both, Rashba-spin-orbit and strain gradient, induce an effective pseudomagnetic field acting with opposite signs on electrons associated with distinct valleys[29]. The strain engendered by the lattice mismatch permeates into the bulk to a depth of approximately the effective lattice constant of the resulting moiré patterns. This depth is estimated to be on the order of 1 nm, significantly smaller than the sample thickness at which the transition manifests and thus consistent with our data. Additionally, it is noted that the coexistence of superconductivity with a different order parameter, such as charge density waves, does not alter the fundamental framework of our phenomenological model. However, it may influence its parameters and serve as a mediator for the interaction between bulk and surface superconducting orders.

The current study identifies a superfluid-density transition that has not been previously observed in transport or tunneling analyses.[3,9,19–21] Notably, previous tunneling investigations were conducted at temperatures of 1.2 K,[3] 300 mK[20] and below 100 mK,[9,21] whereas our experiment was conducted at $T = 4.2$ K. This suggests that the observed transition may be a distinct feature of intermediate temperature regime. While tunneling experiments have also been conducted at $T = 4.2$ K, these were limited to bulk crystals, where suppression of surface states is significant. It is also important to highlight that tunneling experiments using STM cannot fully encapsulate the sample, as the top surface must remain exposed. Our experimental study suggests that encapsulating the sample with hBN on both surfaces might be crucial to prevent degradation and enabling measurement of the intrinsic properties of the sample or to strain the NbSe$_2$ as discussed above. This limitation could be addressed through device-based tunneling experiments, where the top tunneling electrode is deposited on a thin hBN layer. Future SOT measurements at millikelvin temperatures will be necessary to directly compare these results with tunneling experiments.

One might expect that an abrupt change in the superfluid density as a function of film thickness would also manifest in the critical temperature. However, previous transport studies of the T_c thickness dependence revealed only a small change between the bulk value and that observed in 5–6 layer devices.[18] Notably, the ultrathin NbSe$_2$ flakes in Ref. 18 were exfoliated on SiO$_2$ and solely top-encapsulated, while the samples in our study are encapsulated with hBN on both sides. Moreover, assessing T_c in two-dimensional superconductors through transport measurements faces several inherent limitations that are difficult to circumvent. Firstly, these measurements are highly sensitive to the nature of the vortex dynamics and pinning effects[30], which can potentially mask the observed transition, which is measured under

equilibrium conditions. Secondly, transport measurements require metallic leads, which influence the superconducting state through the reverse proximity effect. Thirdly, T_c measurements are sensitive to the order parameter only near the critical temperature, making it impossible to probe transitions occurring at intermediate temperatures as in our experiment.

Measurements of the in-plane critical magnetic field as a function of temperature could provide valuable evidence supporting our findings, provided orbital depairing effects play a significant role. This assumption is plausible, as the zero-temperature out-of-plane coherence length (approximately 2.3 nm[31]) is considerably larger than the interlayer spacing (0.63 nm). Under these conditions, two distinct transitions as a function of the in-plane magnetic field are anticipated: one corresponding to the bulk superconducting order parameter and another, at a higher field, associated with the surface superconducting order parameter.

Such experimental observations have indeed been reported in Ref. 32, where a kink in the critical field versus temperature curve was identified. This kink is interpreted as a first-order transition into a Fulde-Ferrell-Larkin-Ovchinnikov (FFLO) superconducting state. Here, based on our data, we offer an alternative interpretation – namely that the observed kink is in fact the hallmark of the surface superconducting order parameter. Furthermore, consistent with our theoretical explanation, the kink became progressively weaker as the film thickness increased. For films thinner than 5 nm—near the thickness at which we observed the transition—the critical field no longer exhibited the kink associated with the additional transition. These differing interpretations highlight the need for further investigations to distinguish between these scenarios or to reconcile them within a unified framework.

Conclusions

In summary, the present study has unveiled a remarkable anomaly in the Pearl length dependence in the few-layer limit. This anomaly is interpreted as a phase transition in thin films of $NbSe_2$, wherein a reduction in film thickness triggers the suppression of bulk superconductivity, giving rise exclusively to surface superconductivity. Our approach provides invaluable insights into the underlying superconductive characteristics of the system. Specifically, irrespective of the theoretical framework, our experimental methodology serves as a powerful tool for detecting surface superconductivity and the concurrent suppression of bulk superconductivity.

The utility of Pearl-length measurements extends beyond this investigation, as they serve as a sensitive tool for probing the superconducting nature of thin films under various experimental conditions, such as elastic strain, electric field perturbations, or alterations in temperature. This versatility underscores the broader implications of our findings, advancing our understanding of superconductivity in diverse contexts and paving the way for further studies.

Methods

Sample fabrication

hBN was exfoliated onto 285 nm SiO_2/Si substrates, yielding flakes with thicknesses ranging from 5 to 15 nm for the upper layer and 10 to 20 nm for the lower hBN layer. To prepare $NbSe_2$ flakes, an initial exfoliation was carried out onto PDMS, followed by a transfer onto 285 nm SiO_2/Si substrates. This process resulted in the production of large, thin flakes displaying uniform steps. Flakes with consistent and sizable steps were identified utilizing optical microscopy, encompassing various thicknesses. Subsequently, a polycarbonate (PC) pickup technique was employed, as detailed in reference[33]. The pickup started with top hBN, followed by the $NbSe_2$ flake, and finally the lower hBN layer. The resultant structure was positioned onto a SiO_2 chip, near a predeposited gold heater used for SQUID-on-tip localization. Both the pickup procedure and the exfoliation of $NbSe_2$ were executed within an argon environment. This approach aimed to prevent degradation of the samples and maintain their integrity throughout the experimental process.

SQUID-on-tip Fabrication

The SOT was prepared using a self-aligned three-step process involving thermal deposition of Pb at cryogenic temperatures, as outlined in earlier works[16,17]. The SQUID loop employed in this work have a diameter of approximately 250 nm. This choice of a relatively larger diameter is strategic, as it provides the enhanced magnetic sensitivity required for measuring weak extended signals obtained by $\Lambda = 100 \ \mu m$ vortices. Additionally, the larger diameter causes lower period of the quantum interference pattern of the SQUID critical current versus applied field. This enhances the zero-field magnetic sensitivity [16,17], which is essential for measurements at low vortex densities.

SQIUD-on-tip Measurements

All measurements were carried out at a temperature of 4.2 K, which is below the critical temperature of 5.5 K[20] for NbSe2 flakes with three layers or more. To initiate the experimental process, we applied small 0.3 mT magnetic fields to induce the creation of multiple vortices within the sample. Subsequently, we gradually reduced the magnetic field to a range of approximately -0.05 mT to 0.05 mT. Our primary objective during this phase was to identify a relatively isolated vortex positioned at a distance of 1 μm or more from the edges of the uniform steps. Once such a vortex was located, we employed the Tuning fork (TF) to establish a distance akin to that of an AFM. Subsequently, images of these vortices were captured for further analysis.

Sample Characterization

The thicknesses of the $NbSe_2$ flakes were assessed utilizing Scanning Transmission Electron Microscopy (STEM). Specific areas of interest within the sample were carefully selected to encompass the approximate regions where the vortices were observed. These selected areas were subsequently fabricated into thin lamellas using a Focused Ion Beam (FIB) technique. These lamellas were then subjected to STEM imaging, with the outcomes presented in Supplementary Figure 1. To ensure the integrity of the samples, thorough examinations for oxidation and degradation were conducted through Energy Dispersive X-ray Spectroscopy (EDS). The analysis confirmed an organized crystal structure, with no discernible signs of oxidation or degradation.

Tip-to-sample distance measurement

The SOT is attached to a tuning fork excited electrically near its resonance frequency at ~ 32 kHz. The quality factor of the tuning fork coupled with the SOT varies between 10 000 and 30 000 at 4 K with a 10 mbar helium gas pressure. The electrical signal is amplified at room temperature using a homemade operational amplifier. The amplified signal is fed to a nanonis lock-in amplifier in phase-locked loop mode. As the tip approaches within a few nm of the surface, a change in the phase is detected and the tip is retracted by a known safe distance. It was previously calibrated that once the phase variation is detected, the edge of the tip is within 1-2 nm from the sample surface. Thus, the sample-tip distance is set by the distance at which we retract the tip (typically around 300 nm)."

Data availability statement

The data that supports the findings of this study have been deposited in the GitHub database: https://github.com/QIL123/NbSe2_Thin_vortex

Code availability statement

The MATLAB scripts that analyze the raw data and reproduce the figures appearing in this paper have been deposited in the GitHub database: https://github.com/QIL123/NbSe2_Thin_vortex.

Supporting Information

This provides additional experimental and theoretical details that further contribute to the understanding of this study. Specifically, it delves into uncertainty caused by the finite sample size approximation. The vortex analysis and the uncertainty assessment, is covered more extensively, and STEM data is provided.

Author Contributions

Y.A., H.S., O.A., T.D.F., and N.F. conceived the experiment.
A.Z., N.F., T.R.D, E.G, and I.K fabricated the NbSe$_2$ devices.
N.F, and T.D.F conducted the scanning SOT measurements.
O.A. and I.A. conceived the theoretical model.
N.F., T.D.F, A.N, Y.Z and A.G fabricated the SOT sensor.
A.G., and T.D.F fabricated the Tuning forks.
N.F.,T.D.F., and Y.A. generated the numerical simulations.
N.F., T.R.D., A.V., S.R., and T.D.F characterized the NbSe$_2$ samples.
N.F, T.D.F, and M.M. analyzed the data.
Y.A. and A.N. constructed the scanning SOT microscope.
M.E.H. Conceived the SOT readout electronics.
N.F., H.S., O.A., and Y.A. wrote the article with contributions from all authors.

Notes: The authors declare no competing financial interest.

Bibliography

1. Cho, C. W. *et al.* Nodal and Nematic Superconducting Phases in NbSe2 Monolayers from Competing Superconducting Channels. *Phys. Rev. Lett.* **129**, 087002 (2022).

2. Chang, J. *et al.* Direct observation of competition between superconductivity and charge density wave order in YBa2Cu3O6.67. *Nat. Phys.* **8**, 871–876 (2012).

3. Pásztor, Á. *et al.* Multiband charge density wave exposed in a transition metal dichalcogenide. *Nat. Commun.* **12**, 6037 (2021).

4. Yi, M. *et al.* Dynamic competition between spin-density wave order and superconductivity in underdoped Ba1−xKxFe2As2. *Nat. Commun.* **5**, 3711 (2014).

5. Keimer, B., Kivelson, S. A., Norman, M. R., Uchida, S. & Zaanen, J. From quantum matter to high-temperature superconductivity in copper oxides. *Nature* **518**, 179–186 (2015).

6. Zhou, X. *et al.* High-temperature superconductivity. *Nat. Rev. Phys.* **3**, 462–465 (2021).

7. Cao, Y. *et al.* Nematicity and competing orders in superconducting magic-angle graphene. *Science* **372**, 264–271 (2021).

8. Gor'kov, L. P. & Rashba, E. I. Superconducting 2D System with Lifted Spin Degeneracy: Mixed Singlet-Triplet State. *Phys. Rev. Lett.* **87**, 037004 (2001).

9. Guillamón, I. *et al.* Superconducting Density of States and Vortex Cores of 2H- NbS2. *Phys. Rev. Lett.* **101**, 166407 (2008).

10. Edkins, S. D. *et al.* Magnetic field–induced pair density wave state in the cuprate vortex halo. *Science* **364**, 976–980 (2019).

11. Iguchi, Y. *et al.* Superconducting vortices carrying a temperature-dependent fraction of the flux quantum. *Science* **380**, 1244–1247 (2023).

12. Maggio-Aprile, I. *et al.* Vortex-core spectroscopy of d-wave cuprate high-temperature superconductors. *Phys. C Supercond. its Appl.* **615**, 1354386 (2023).

13. Pearl, J. Current distribution in superconducting films carrying quantized fluxoids. *Appl. Phys. Lett.* **5**, 65 (1964).

14. Tafuri, F., Kirtley, J. R., Medaglia, P. G., Orgiani, P. & Balestrino, G. Magnetic imaging of pearl vortices in artificially layered (Ba 0.9Nd0.1CuO2+x)m/(CaCuO 2)n systems. *Phys. Rev. Lett.* **92**, 157006 (2004).

15. Thiel, L. *et al.* Quantitative nanoscale vortex imaging using a cryogenic quantum magnetometer. *Nat. Nanotechnol.* **11**, 677–681 (2016).

16. Vasyukov, D. *et al.* A scanning superconducting quantum interference device with single electron spin sensitivity. *Nat. Nanotechnol.* **8**, 639–644 (2013).

17. Anahory, Y. *et al.* SQUID-on-tip with single-electron spin sensitivity for high-field and ultra-low temperature nanomagnetic imaging. *Nanoscale* **12**, 3174–3182 (2020).

18. Xi, X. *et al.* Ising pairing in superconducting NbSe2 atomic layers. *Nat. Phys.* **12**, 139–143 (2016).

19. Noat, Y. *et al.* Quasiparticle spectra of 2H-NbSe2: Two-band superconductivity and the role of tunneling selectivity. *Phys. Rev. B* **92**, 134510 (2015).

20. Khestanova, E. *et al.* Unusual Suppression of the Superconducting Energy Gap and Critical Temperature in Atomically Thin NbSe2. *Nano Lett.* **18**, 2623–2629 (2018).

21. Kuzmanović, M. *et al.* Tunneling spectroscopy of few-monolayer NbSe2 in high magnetic fields: Triplet superconductivity and Ising protection. *Phys. Rev. B* **106**, 184514 (2022).

22. de Trey, P., Gygax, S. & Jan, J. P. Anisotropy of the Ginzburg-Landau parameter κ in NbSe2. *J. Low Temp. Phys.* **11**, 421–434 (1973).

23. Takita, K. & Masuda, K. Charge density wave transition and superconductivity in 2H-NbSe2. Direct measurement of the penetration depth in a layered superconductor. *J. Low Temp. Phys.* **58**, 127–142 (1985).

24. Le, L. P. *et al.* Magnetic penetration depth in layered compound NbSe2 measured by muon spin relaxation. *Phys. C Supercond.* **185**–**189**, 2715–2716 (1991).

25. Talantsev, E. F. *et al.* On the origin of critical temperature enhancement in atomically thin superconductors. *2D Mater.* **4**, 025072 (2017).

26. Dvir, T. *et al.* Spectroscopy of bulk and few-layer superconducting NbSe2 with van der Waals tunnel junctions. *Nat. Commun.* **9**, 598 (2018).

27. Wang, H. *et al.* High-quality monolayer superconductor NbSe2 grown by chemical vapour deposition. *Nat. Commun.* **8**, 394 (2017).

28. Han, T. *et al.* Investigation of the two-gap superconductivity in a few-layer NbSe2-graphene heterojunction. *Phys. Rev. B* **97**, 060505 (2018).

29. Bir, G. L. Symmetry and strain-induced effects in semiconductors. (1974).

30. Feigel'man, M. V., Geshkenbein, V. B. & Larkin, A. I. Pinning and creep in layered superconductors. *Phys. C Supercond.* **167**, 177–187 (1990).

31. Nader, A. & Monceau, P. Critical field of 2H-NbSe2 down to 50mK. *Springerplus* **3**, 16 (2014).

32. Wan, P. *et al.* Orbital Fulde–Ferrell–Larkin–Ovchinnikov state in an Ising superconductor. *Nature* **619**, 46–51 (2023).

33. Zomer, P. J., Guimarães, M. H. D., Brant, J. C., Tombros, N. & Van Wees, B. J. Fast pick up technique for high quality heterostructures of bilayer graphene and hexagonal boron nitride. *Appl. Phys. Lett.* **105**, 013101 (2014).

Supplementary Information

Anomalous Thickness Dependence of the Vortex Pearl Length in Few-Layer NbSe$_2$

Nofar Fridman[1,2*], Tomer Daniel Feld[1,2], Avia Noah[1,2],Ayelet Zalic[1,2], Maya Markman[1,2],T.R Devidas[1,2], Yishay Zur[1,2], Einav Grynszpan[1,2], Alon Gutfreund[1,2], Itay Keren[1,2], Atzmon Vakahi[2], Sergei Remennik[2], Kenji Watanabe[3], Takashi Taniguchi[3] , Martin Emile Huber[4], Igor Aleiner[5], Hadar Steinberg[1,2], Oded Agam[1*], Yonathan Anahory[1,2*]
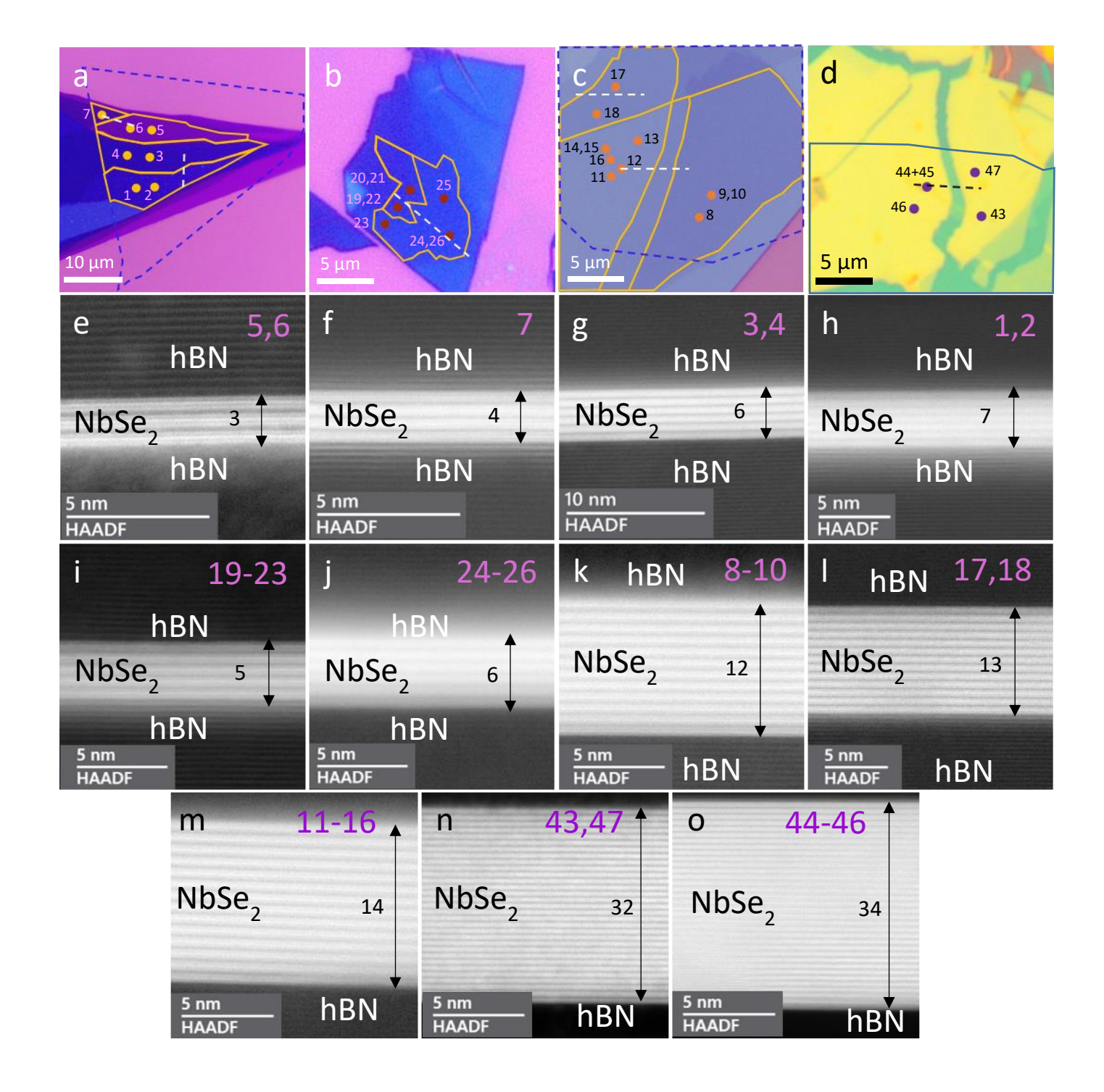
[1] The Racah Institute of Physics, The Hebrew University, Jerusalem, 9190401, Israel
[2] Center for Nanoscience and Nanotechnology, Hebrew University of Jerusalem, Jerusalem, 9190401, Israel
[3] Research Center for Electronic and Optical Materials, National Institute for Materials Science, 1-1 Namiki, Tsukuba 305-0044, Japan
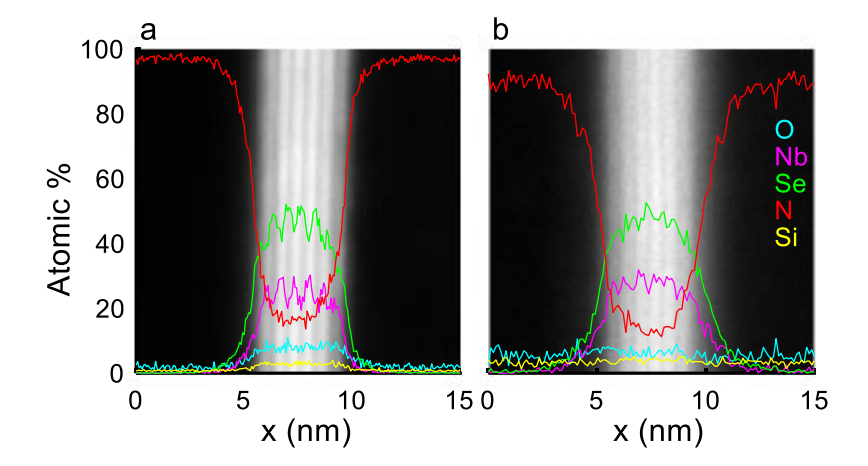[4] Departments of Physics and Electrical Engineering, University of Colorado Denver, Denver, CO 80217, USA
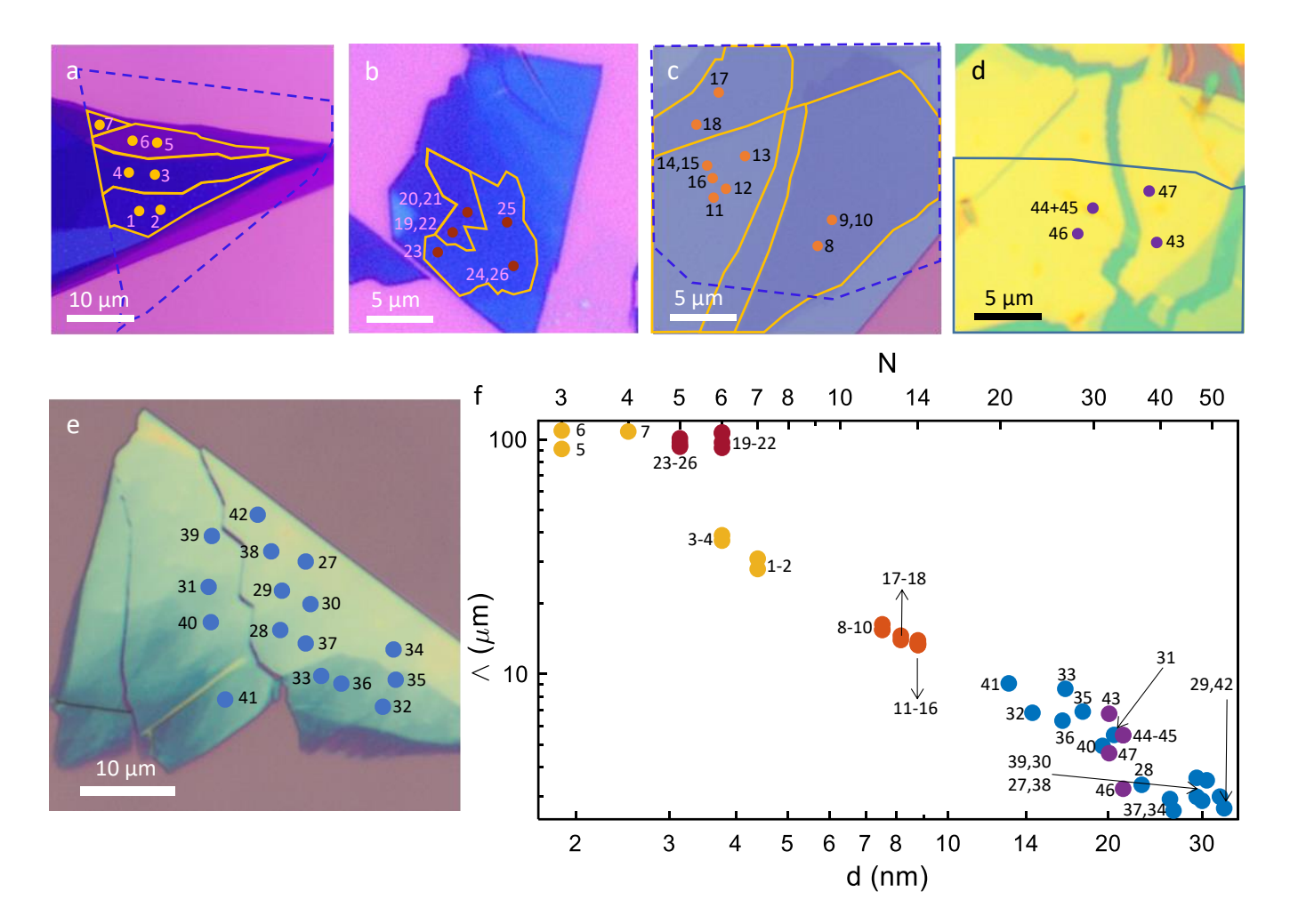[5] Google Quantum AI, Santa Barbara, CA, USA
* Corresponding authors
nofarfri.friedman@mail.huji.ac.il ,yonathan.anahory@mail.huji.ac.il, agam.oded@gmail.com

Supplementary Figure 1. Cross-sectional TEM images

(**a-d**) Optical images of the NbSe$_2$ thin flakes measured in this work. Dots on the images indicate the positions of the measured vortices, with numerical labels used to identify the vortex in further figures. Yellow outlines delineate the edges of the NbSe$_2$ terraces. White and black dashed lines in **a-c** and **d**, respectively, indicate the sections chosen for TEM cross-sectional analysis. In panels **a** and **c**, a dashed blue line demarcates the region of double encapsulation by hBN. (**b**) The entire field of view is encapsulated with top and bottom hBN. (**d**) Image of an encapsulated NbSe$_2$ in which the yellow region denotes the doubly encapsulated region, and the blue line shows the edge of the NbSe$_2$ flake. (**e-o**) Cross-sectional TEM images of the NbSe$_2$ flakes shown in **a-d** along the dashed lines. The numbers in purple correspond to the vortex labels in panels **a-d**. (**e-h**) TEM images taken from the sample shown in **a**, containing $N = 3, 4, 6$ and 7 layers, respectively. (**i-j**) TEM images taken from the sample shown in **b**, containing $N = 5$ and 6 layers, respectively. (**k-m**) TEM images taken from the sample shown in **c**, containing $N = 12, 13$ and 14 layers, respectively. (**n-o**) TEM images taken from the sample shown in **d**, containing $N = 32$ and 34 layers, respectively.
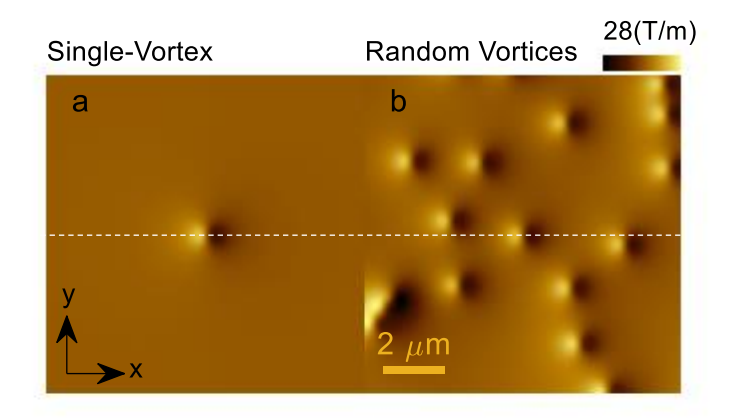
Supplementary Figure 2 Energy-dispersive X-ray spectroscopy chemical composition profile.
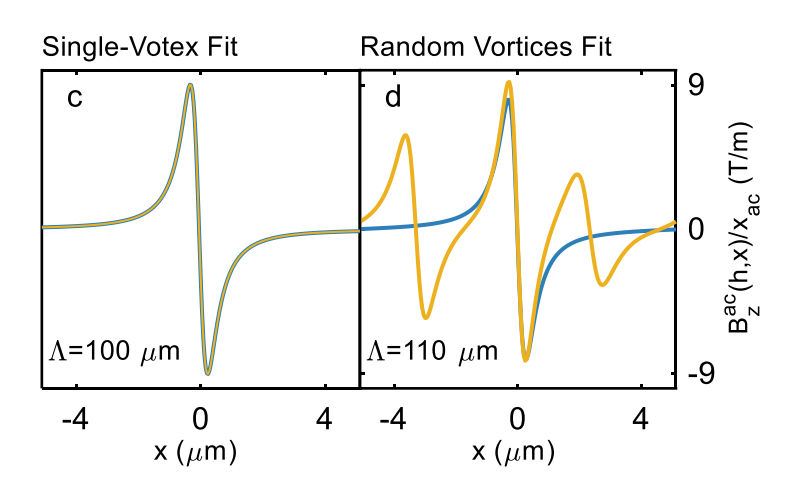
(**a-b**) Typical profile of the relative atomic percentage of the following elements Nb,Se,N,O and Si, corresponding to the cross sections shown in Supplementary Figure 1.a-b, respectively. Oxygen and nitrogen contamination is visible throughout the layers. Oxygen contamination is attributed to the air exposure upon lamella preparation while nitrogen is attributed to the layer intermixing caused by the Ga FIB during the lamella preparation. No surface contamination was detected.

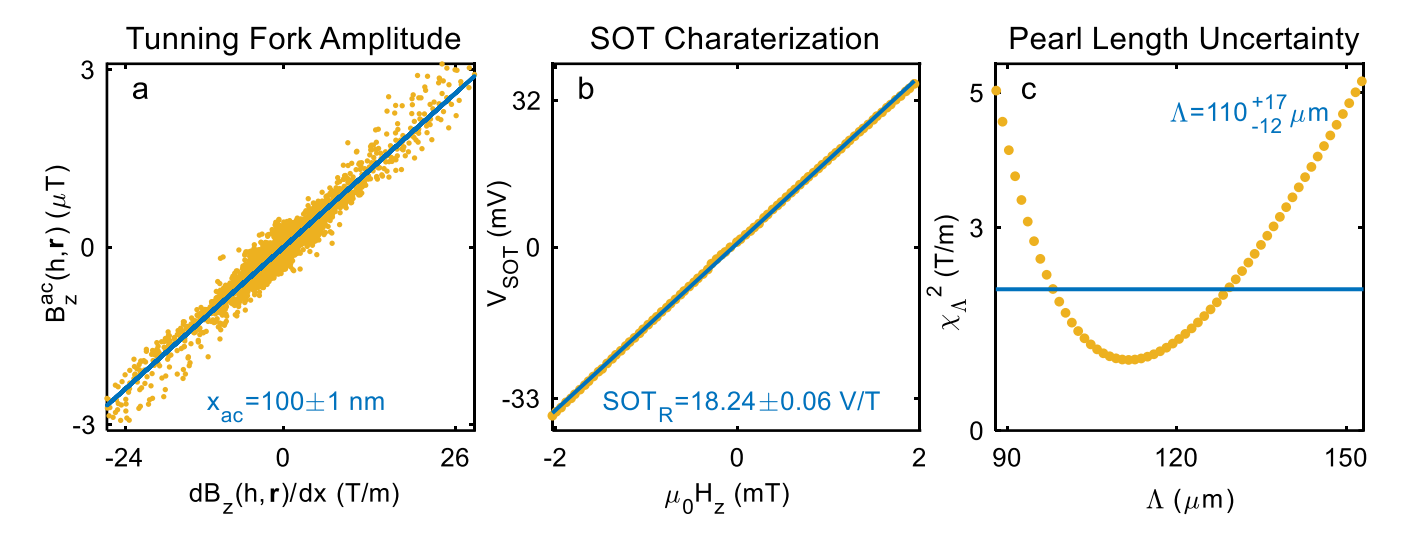**Supplementary Figure 3. Samples and Vortex Locations**

(**a-e**) Optical images of all the flakes measured in this work. Dots mark the locations where vortices were imaged and numbers near them is the vortex number shown in **f**. (**a,c**) The edges of the terraces are delineated by yellow lines, and the dashed blue lines show the sample's area covered with top and bottom hBN.(**b**) The entire field of view is encapsulated with top and bottom hBN. (**d**) Image of an encapsulated NbSe$_2$. The yellow region is the doubly encapsulated region, and the blue line shows the edge of the NbSe$_2$ flake. (**e**) NbSe$_2$ flake that was not encapsulated. (**f**) The measured values of the Pearl length Λ as a function of the sample thickness d for all vortices shown in this work. The number near each data point is the vortex number shown in images **a-e**. Point color relates to the optical image from which the data point was acquired; yellow **a**, red **b**, orange **c**, purple **d**, and blue **e**.
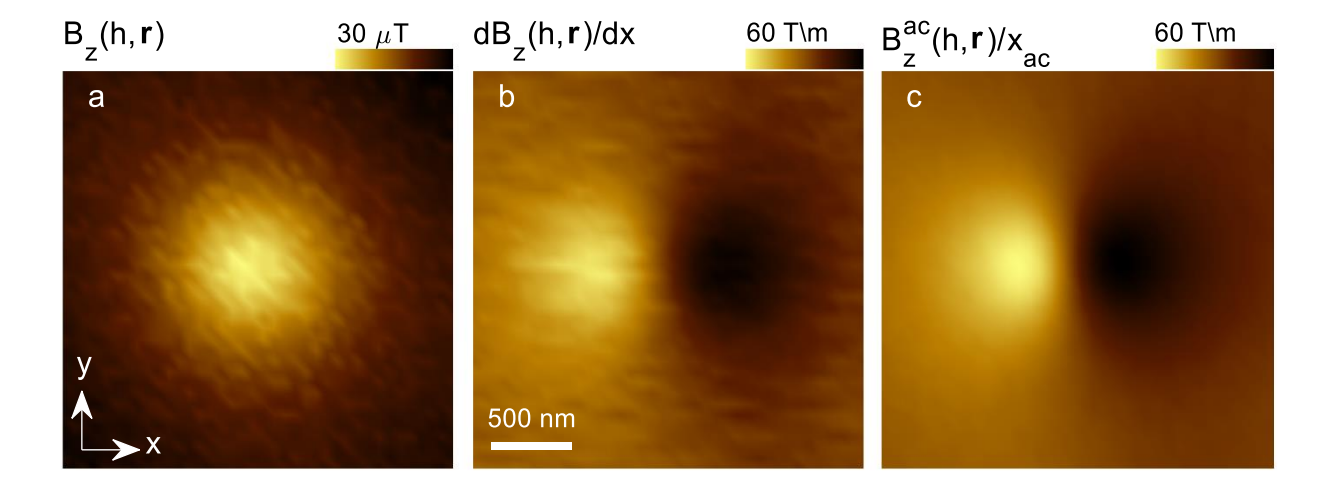
Supplementary Figure 4. The influence of nearby vortices on the Pearl length Λ

(**a,b**) Calculated theoretical spatial derivative along the x axis of the out-of-plane component of magnetic field $\frac{dB_z(h,\boldsymbol{r})}{dx}$ of vortices with Pearl length of $\Lambda = 100$ μm, where $h = 360$ nm is the distance from the tip-to-surface distance and $\boldsymbol{r} = (x,y)$ is the in-plane coordinate. The white dashed line marks the location of the cross-sections shown in panels **c,d**. (**a**) The analytical gradient of the magnetic field for a single vortex. (**b**) Multi-vortex simulation with average vortex spacing of 2 μm. (**c,d**) Cross-sections of the calculated magnetic field derivative along the white dashed line shown in panels **a,b** and their respective fits. The single-vortex fit gives $\Lambda = 100$ μm, while the fit for the multi-vortex situation yields $\Lambda = 110$ μm. Thus, the change in the Pearl Length due to nearby vortices is around 10%.

Supplementary Figure 5. Measurement error sources

(**a**) Tuning fork amplitude determination: A scatter plot of the data for the out-of-plane component of magnetic field $B_z^{ac}(h, \mathbf{r})$ and $\frac{dB_z(h,\mathbf{r})}{dx}$ (yellow dots) together with the best fit for the oscillation amplitude x_{ac} (blue line) as discussed in Supplementary Note 2, see Eq.(14). Here, h is tip-to-sample distance and $\mathbf{r} = (x, y)$ the inplane coordinate (**b**) Determination of SOT response coefficient - SOT_R. The measured voltage as a function of the magnetic field (yellow dots) and corresponding linear fit (blue line). The slope is SOT_R. (**c**) An example for the error analysis performed for vortex No. 6 shown in Supplementary Figure 3a,f, which corresponds to $N = 3$ layers. This panel shows the residual difference between modeled and measured image χ_Λ^2 as a function of the Pearl Length values (yellow dots) as discussed in Supplementary Note 3 and Eq. (13). $\chi_\Lambda^2 = 2 \cdot \chi_{\Lambda\text{min}}^2$ (blue line), which determines one standard deviation σ_Λ.

Supplementary Figure 6. Determination of the tuning fork amplitude

(**a**) SQUID-on-tip (SOT) image of the out-of-plane component of the magnetic field $B_z(h, \boldsymbol{r})$ of an isolated vortex located in the $N = 7$ layer region shown in Supplementary Figure 3a,f and referred as vortex No. 2. Here h is the tip-to-sample distance and $\boldsymbol{r} = (x, y)$ is the in-plane coordinate. This image was obtained at $\mu_0 H_z = 60\ \mu\mathrm{T}$ with $h = 360$ nm. The signal from this vortex ($\Lambda = 30\ \mu$m) is sufficiently large to measure in dc mode allowing us to determine the oscillation amplitude of the SQUID loop x_{ac} .(**b**) Numerical derivative of **a** along the x axis $\frac{dB_z(h,r)}{dx}$. (**c**) The in-phase component of the magnetic field oscillating at the tuning fork frequency $B_z^{ac}(h, \boldsymbol{r})$ and divided by the oscillation amplitude x_{ac}.This amplitude is the factor between the signals presented in panels **b** and **c**, and is determined through the scatter plot presented in Supplementary Figure 5a.

Supplementary Note 1: Magnetostatics of Finite Superconducting Films

In this section, our aim is to justify the approximations employed for the quantitative analysis of the magnetic field distribution. The main assumption hinges on the sample's size, L, being significantly smaller than the Pearl length, Λ, while also being much larger than the distance, h, between the squid tip and the sample surface.

Excluding the region of the superconducting film, which is assumed to be situated on the plane $z = 0$ and its thickness is disregarded, a static magnetic B satisfies the Maxwell equations in vacuum:

$$\nabla \cdot \boldsymbol{B} = 0 \quad \text{and} \quad \nabla \times \boldsymbol{B} = 0. \tag{1}$$

However, the finite 2-dimensional current density J_α within the film, where $\alpha = x, y$ represents the coordinates on the film plane, causes a discontinuity in the planar components of the magnetic field, $\boldsymbol{B}$, across this plane:

$$
\begin{aligned}
\Delta B_x &= \mu_0 J_y, \\
\Delta B_y &= -\mu_0 J_x,
\end{aligned}
\tag{2}
$$

where $\Delta \boldsymbol{B} = \boldsymbol{B}\big|_{z=0^+} - \boldsymbol{B}\big|_{z=0^-}$. It is convenient to define the dual counterpart of the current density vector, acquired through a 90-degree rotation, $\boldsymbol{J}^D = \hat{z} \times \boldsymbol{J}$. This dual current density can be represented as $\boldsymbol{J}^D = \rho_s \boldsymbol{v}^D$, where ρ_s is the two-dimensional superfluid density and $\boldsymbol{v}^D$ is the dual superfluid velocity. Conservation of current implies that

$$\nabla \cdot \boldsymbol{J} = \nabla \times \boldsymbol{J}^D = 0. \tag{3}$$

The dual superfluid velocity describes all quantum aspects of the superfluid current within the system:

$$\partial_\alpha v_\alpha^D = 2\pi \left[\sum_j \delta^{(2)}\left(\boldsymbol{r} - \boldsymbol{r}_j\right) - \frac{B_z}{\phi_0} \right]. \tag{4}$$

Here $\boldsymbol{r}_j$ are the position coordinates of the vortices in the film (all assumed to have the same vorticity), and ϕ_0 is the superconducting flux quantum. Equation (4) can be derived by variation of the Ginzburg-Landau energy functional after applying the Madelung transformation, $\psi = \sqrt{\rho_s} \exp(i\theta)$, and identifying the velocity as the gradient of the phase, $\boldsymbol{v} = \nabla\theta$. This equation expresses the fact that the circulation of the current arises solely from the presence of vortices or from the Aharonov-Bohm effect. If the film is of infinite size in the planar direction and the variations in ρ_s are neglected, a straightforward calculation of the Fourier transform of the component of the magnetic field that is perpendicular to the film,

$$\hat{B}_z(z, \boldsymbol{q}) = \int d^2 r \exp(-i\boldsymbol{q} \cdot \boldsymbol{r}) B_z(z, \boldsymbol{r}) \tag{5a}$$

yields[2]

$$\hat{B}_z(z, \boldsymbol{q}) = \hat{B}(\boldsymbol{q}) \exp(-q|z|), \quad \text{with} \quad \hat{B}(\boldsymbol{q}) = \frac{\phi_0}{\Lambda q + 1} n_V(\boldsymbol{q}), \tag{5b}$$

where $n_V(\boldsymbol{q}) = \sum_j \int d^2 r \exp(-i\boldsymbol{q} \cdot \boldsymbol{r}_j)$ is the Fourier transform of the vortex density, $q = |\boldsymbol{q}|$, and the Pearl length Λ is given by

$$\frac{1}{\Lambda} = \frac{\pi \rho_s \mu_0}{\phi_0}. \tag{6}$$

The finite size of the system presents a challenge when calculating the effects of the boundary currents, but at the same time, it allows for simplifying the problem. Specifically, when the magnetic field is sufficiently weak such that $\Lambda \gg L$, Eq. (4) can be approximated by

$$\partial_\alpha v_\alpha^D = 2\pi \sum_j \delta^{(2)}\left(\boldsymbol{r} - \boldsymbol{r}_j\right), \tag{7}$$

and neglecting variations of ρ_s within the sample implies that Eq. (3) reduces to

$$\nabla \times \boldsymbol{v}^D = 0. \tag{8}$$

Furthermore, the condition for no direct current flow through the system's boundary translates into the condition that the dual velocity is perpendicular to the boundary - hereinafter denoted by Γ. Therefore, the solution of Eqs. (7) and (8) can be found from the solution for the two-dimensional Poisson's equation for the velocity potential, Φ:

$$\nabla^2 \Phi = 2\pi \sum_j \delta^{(2)}\left(\mathbf{r} - \mathbf{r}_j\right) \quad \text{where} \quad v_\alpha^D = \partial_\alpha \Phi, \tag{9}$$

and with Dirichlet boundary conditions, $\Phi|_{r\in\Gamma} = 0$. The solution of this equation is given by:

$$\Phi(\mathbf{r}) = \sum_j \ln\left|\mathbf{r} - \mathbf{r}_j\right| - \oint_\Gamma dl\, \hat{\mathbf{n}}' \cdot \mathbf{v}^D(\mathbf{r}') \ln\left|\mathbf{r} - \mathbf{r}'\right|, \tag{10}$$

where dl is an infinitesimal length element along the boundary, while $\hat{\mathbf{n}}'$ is a unit vector normal to the boundary at point $\mathbf{r}'$ that resides on the boundary, and pointing outwards. The dual current on the boundary, $\mathbf{v}^D(\mathbf{r}')$, should be found from the solution of integral equation derived from Eqs. (8-10) with Dirichlet boundary conditions $\Phi|_{r\in\Gamma} = 0$. The solution of this equation is complicated for the sample shapes used in the experiments. Nevertheless, for the interpretation of the experimental data, $\mathbf{J}^D(\mathbf{r})$ is not required, as we explain below.

Solution of Eqs. (1-3) and (7-8) is explicitly given by a sum of two component:

$$B_z(h,\mathbf{r}) = B_z^{(1)} + B_z^{(2)}, \tag{11a}$$

where

$$B_z^{(1)} = \frac{\phi_0}{2\pi\Lambda} \sum_j \frac{1}{\sqrt{h^2 + \left(\mathbf{r} - \mathbf{r}_j\right)^2}}, \tag{11b}$$

is the contribution from vortices, while

$$B_z^{(2)} = -\frac{\phi_0}{2\pi\Lambda} \sum_j \oint_\Gamma \frac{dl\, \hat{\mathbf{n}}' \cdot \mathbf{v}^D(\mathbf{r}')}{\sqrt{h^2 + \left(\mathbf{r} - \mathbf{r}'\right)^2}} \tag{11c}$$

is the magnetic field generated by boundary currents. A comparison of the vortex contribution (11b) with the boundary term (11c) suggests a procedure by which the latter is eliminated. It is achieved by considering the gradients of $B_z(\mathbf{r})$ rather than the field itself. Indeed, estimation from Eqs. (11) yield

$$\frac{\max\left\|\partial_x B^{(2)}\right\|}{\max\left\|\partial_x B^{(1)}\right\|} \simeq \frac{h^2}{L^2}, \tag{12}$$

where L is the linear size of the system that satisfies the condition, $h \ll L \ll \Lambda$. Here it is assumed that the vortex distance from the boundary (or other vortices) is of order L. This result means that for the purpose of extracting the Pearl length from a χ^2 fit (described in the next section) one can ignore the boundary contribution and use only the contribution associated with a single vortex.

Supplementary Note 2: Quantitative Analysis of the Pearl Vortices

We employ the least squares method[1] to determine the Pearl length Λ from our SOT images. We numerically minimize the parameter χ^2 which is given by:

$$\chi^2 = \sum_{i=1}^{N_{pixel}} \left(\frac{dB_z(h,\mathbf{r}_i)}{dx} - \frac{dB_z^{th}(h,\mathbf{r}_i)}{dx} \right)^2 , \tag{13}$$

where $dB_z(h,\mathbf{r})/dx$ is the spatial derivative of the out-of-plane component of the magnetic field emanating from the vortex, $dB_z^{th}(h,\mathbf{r})/dx$ is the theoretical spatial derivative of the magnetic field calculated using the Pearl model, and the sum is over all the pixels of the image in which $\mathbf{r}_i$ denotes the position corresponding to the ith pixel.

The magnetic field derivative is directly measured by sensing the oscillating component of the magnetic field, $B_z^{ac}(h,\mathbf{r})$, caused by an in-plane oscillation of the SQUID loop. We divide this signal by the oscillation amplitude x_{ac} to obtain the derivative. Using this measurement technique has many benefits, as discussed in the main text. The oscillation amplitude, x_{ac}, is determined using the following relation:

$$\frac{dB_z(h,\mathbf{r})}{dx} \simeq \frac{B_z^{ac}(h,\mathbf{r})}{x_{ac}} , \tag{14}$$

for an image with a strong gradient as illustrated in supplementary figure 6. This image can be, for example, a vortex with a $\Lambda \lesssim 30$ μm. We find the proportional constant that satisfies equation (14) by calculating numerically the gradient of the dc image $dB_z(h,\mathbf{r})/dx$ (supplementary figure 6b) and comparing it to the measured $B_z^{ac}(h,\mathbf{r})$ using a lock-in amplifier (Supplementary Figure 6c). For a given set of measurements, the oscillation amplitude is constant within 2%. The difference between measurement and the theoretical formula in Eq. (13) is performed for every pixel for the entire image containing N_{pixel} pixels.

The starting point for calculating $dB_z^{th}(h,\mathbf{r})/dx$ is the formula for the magnetic field of a single Pearl vortex, which in Fourier space is given by Eq. (5b) with $n_v(\mathbf{q}) = 1$. This expression is transformed into real space and differentiate with respect to x. The resulting expression is calculated for the same number and size of pixels as our SOT image. This analysis yields the Pearl length values for all the vortices, plotted as a function of thicknesses, as shown in Figure 4.

Supplementary Note 3: Quantitative Analysis of Pearl Length Uncertainties

There are two relevant measured quantities in this work: the sample thickness N and the Pearl length Λ. In the following, we estimate their respective uncertainties.

3.1 Uncertainty on the Pearl length Λ

The following uncertainty estimation takes into consideration the uncertainty inherent to each measured parameter required to compare the measured signal (in volts) with the model (section 3.1.1 below). Another contribution to the uncertainty is related to the signal-to-noise ratio and other imaging artefacts (section 3.1.2 below).

3.1.1 Input parameter uncertainty

The delta method[3] serves to evaluate the uncertainty on the Pearl Length given the uncertainty on other measured parameters. The method relies on prior measurements of each parameter s_i, and its uncertainty σ_{s_i}. These parameters are the SQUID Tesla-to-Volt transfer function SOT_R, the SQUID loop in-plane oscillation amplitude x_{ac} and the distance between the SQUID loop and the surface of the sample h. To calculate the resulting uncertainty on Λ, each parameter is individually perturbed by one standard deviation $\pm\sigma_{s_i}$ as follows:

$$\Delta\widehat{\Lambda}_1 = \widehat{\Lambda}(s_1 \pm \sigma_1, s_2, s_3) - \widehat{\Lambda}(s_1, s_2, s_3) \tag{15}$$

Here $\Delta\widehat{\Lambda}_1$ represents the uncertainty arising from perturbing s_1. The total uncertainty on Λ is obtained by summing in quadrature the uncertainty resulting from each parameter:

$$\left(\Delta\widehat{\Lambda}_{tot}\right)^2 = \sum_i\left(\Delta\widehat{\Lambda}_i\right)^2 \tag{16}$$

We now discuss the uncertainty evaluation of each relevant parameter.

The transfer function SOT_R is determined by calibrating the SQUID voltage response to a known change in the magnetic field (Supplementary Figure 5b). The uncertainty on this parameter is caused by statistical fluctuations in the measurement, as shown in Supplementary Figure 5b. For example, the calibration obtained while measuring vortex 6 has an estimated uncertainty of 2%, which translates into an uncertainty of 2 μm (2%) in the measurement of $\Lambda = 111$ μm.

The method used to determine x_{ac}, and its associated uncertainty is described in Supplementary Note S2 and shown in Supplementary Figure 5a. The uncertainty on this parameter is caused by statistical fluctuations in the measurement, as shown in Supplementary Figure 5a. For example, the uncertainty on x_{ac} for vortex 6 is estimated to be 1%, which corresponds to 1 μm (1%) uncertainty in the measurement of Λ.

The distance between the tip and sample h is determined by employing the tuning fork to sense the sample surface, akin to an AFM operation. We approximate its uncertainty to be ±15 nm, factoring the uncertainty on the thickness of the hBN layer covering the sample and other surface impurities (10 nm). We also consider the statistical variance of the surface sensing, which exhibited variations within ±10 nm. This uncertainty for vortex 6 translates into $\Lambda = 111^{+8}_{-7}$ μm.

The total uncertainty is calculated for each vortex separately and can vary, but they are typically around ~9%, and the main contribution is the uncertainty on h.

3.1.2 Uncertainty caused by the image signal-to-noise ratio and other imaging artefacts

As explained in note 2, the least squares method minimizes the difference between the magnetic profile of the modeled and the measured vortex. Given the noise in our measurements and other imaging artifacts discussed below, the smallest residual is $\chi^2_{min} > 0$. We calculate the interval of confidence for Λ (within one standard deviation $\pm\sigma$) by considering the range of Λ for which $\chi^2 < 2 \times \chi^2_{min}$.[1] Supplementary Figure 5c shows a typical example of χ^2 as a function of Λ for a particular vortex (vortex number 6). From this graph, we estimate the uncertainty, which typically is +16/-11 % for vortices of low signal ($N < 10$).

Another uncertainty stems from imaging artefacts that are unaccounted in the Pearl model. We consider two main sources of unaccounted background. The presence of vortices and the presence of edges near the vortex of interest. These two sources have the same effect but with opposite sign given that the boundary conditions caused by the edge is modeled by a mirror image vortex. The influence of nearby vortices is shown in Supplementary Figure 4a-d where we simulate a sample with $\Lambda = 100$ μm in presence of other vortices at the same distance we would encounter in a real experiment. The result is an enlargement of Λ of typically 10%. Consequently, edges located at the same distance from the vortex of interest would have the opposite effect of shrinking Λ by 10%.

3.1.3 Uncertainty on the tip diameter

The uncertainty of the tip diameter influences the measured Λ because the image resulting from the Pearl model is convoluted with the tip size to account for finite tip-size smoothing. We note that the convolution method is only sensitive to a change in diameter greater than the pixel size (60 nm). The tip diameter was determined by measuring the field period of the SQUID interference pattern ΔH_z. Knowing that one period corresponds to a change in flux corresponding to the flux quantum Φ_0, we can state that $\pi r^2 \Delta H_z = \Phi_0$. The uncertainty of the field period is small (a few percent). In principle, other effects, such as flux focusing, could change the effective diameter. However, such an effect was never observed on a magnitude comparable with the pixel size (Ref. 16 and 17 of the main text). The negligible influence is most likely due to the thin film geometry found in the SOT. For those reasons, we consider the uncertainty on the tip diameter as negligible.

3.1.4 Summing all uncertainties

Here we present a table of the average parameter uncertainties and their resultant Pearl uncertainties:

Parameter Names	Input Parameters			Fitting Uncertainty	Environment Artefacts	
	SOT_R	x_{ac}	h	Λ	Boundary Conditions	Surrounding Vortices
Parameter Uncertainty %	±2	±2	±5			
Resultant Pearl Positive Uncertainty %	2	2	9	16	0	10
Resultant Pearl Negative Uncertainty %	2	2	8	11	10	0

Finally, the sum of all the uncertainties takes the following form:

$$\Delta_{\Lambda tot}^{Lower\ Boundary} = \sqrt{\Delta_{Input\ ParametersLB}^2 + \Delta_{\Lambda LB}^2 + \Delta_{surrounding\ verticesLB}^2 + \Delta_{boundary\ conditionsLB}^2} = \sqrt{8^2 + 12^2 + 0^2 + 11^2}$$
$$= 18\ \mu m$$

$$\Delta_{\Lambda tot}^{Upper\ Boundary} = \sqrt{\Delta_{Input\ ParametersUB}^2 + \Delta_{\Lambda UB}^2 + \Delta_{surrounding\ verticesUB}^2 + \Delta_{boundary\ conditionsUB}^2} = \sqrt{9^2 + 17^2 + 11^2 + 0^2}$$
$$= 22\ \mu m$$

$\Delta_{\Lambda tot}^{Lower\ Boundary}$ and $\Delta_{\Lambda tot}^{Upper\ Boundary}$ indicate the lower and upper limits. As, the presence of neighboring vortices, results in a positive deviation thus, they contribute to the upper limit. Conversely, the boundary conditions contribute as negative vortices and are thus relevant to the lower limit. The final result here is:

$$\Lambda_6 = 111_{-18}^{+22}\ \mu m$$

The same type of calculation is conducted for each vortex and gives the error bars shown in Fig. 4. Λ_6 depicts the full uncertainty calculation for a vortex residing in the 3 layer region. The average uncertainties of Pearl lengths are given in the table above.

3.2 Uncertainty of the sample thickness

Finally, we address the evaluation of thickness uncertainties. The flakes under consideration, with the exception of the one featured in Supplementary Figure 3e, exhibited thickness uniformity across the measurement steps, as ascertained via TEM (Supplementary Figure 1), resulting in no uncertainties.

For the specific flake showcased in Supplementary Figure 3e, thicknesses were determined using AFM images. This particular flake displayed less uniform steps and was not covered with hBN, leading to associated thickness uncertainties. To gauge these uncertainties, AFM scans were conducted over a region of approximately 1 µm in diameter surrounding the vortex location. The assigned thickness was established as the average thickness, and its uncertainty is assigned as the standard deviation $d_i + \Delta d_i$. For this sample, the typical uncertainty in thickness was 10%.

Supplementary References

1. James, G., Witten, D., Hastie, T., Tibshirani, R. & Taylor, J. *An Introduction to Statistical Learning*. Springer

International Publishing, 72-78 (2023).

2. Pearl, J. Current distribution in superconducting films carrying quantized fluxoids. *Appl. Phys. Lett* **5**, 65 (1964).

3. Cox, C. Fieller's Theorem, the Likelihood and the Delta Method. *Biometrics* **46**, 709 (1990).